Ultralow overpotential nitrate reduction to ammonia via a three step relay mechanism

Shuhe Han
Tianjin University https://orcid.org/0000-0002-0514-5669
Hongjiao Li
School of Chemical Engineering, Sichuan University https://orcid.org/0000-0002-0388-6818
Tieliang Li
Tianjin University https://orcid.org/0000-0001-6936-1750
Fanpeng Chen
Tianjin University https://orcid.org/0000-0003-2684-3180
Rong Yang
Tianjin University
Yifu Yu
Tianjin University https://orcid.org/0000-0002-7927-1350
Bin Zhang (bzhang@tju.edu.cn)
Tianjin University https://orcid.org/0000-0003-0542-1819

Article

Keywords:

Posted Date: February 20th, 2023

DOI: https://doi.org/10.21203/rs.3.rs-1550500/v1

Version of Record: A version of this preprint was published at Nature Catalysis on April 20th, 2023. See the published version at https://doi.org/10.1038/s41929-023-00951-2.

Abstract

Ammonia plays a significant role in agriculture and the next-generation carbon-free energy supply. Electrocatalytic nitrate reduction to NH_3 is attractive for nitrate removal and NH_3 production under ambient conditions. However, the energy efficiency is limited by the high reaction overpotential. Here, we propose a three-step relay mechanism composed of a spontaneous redox reaction, electrochemical reduction, and electrocatalytic reduction to overcome this issue. Ru_xCo_y alloys are designed and adopted as model catalysts. $Ru_{15}Co_{85}$ exhibits an onset potential of +0.4 V versus a reversible hydrogen electrode and an energy efficiency of 41.54 ± 1.72 %, which are both the best records. The high performance results in a low production cost of \$0.49 ± 0.02 /$kg_{ammonia}$ (\$0.58~1.02/$kg_{ammonia}$ sold in the USA). Electrochemical *in situ* spectroscopy and theoretical simulations indicate that the three-step relay mechanism leads to excellent catalytic performance on $Ru_{15}Co_{85}$ and can be extended to Ru_xFe_y and Ru_xNi_y alloys.

Introduction

Ammonia (NH_3), as one of the most common industrial chemicals, is essential for the production of nitrogenous fertilizers and shows great promise as a next-generation hydrogen-rich fuel.[1-3] NH_3, with an annual global market of 150 million metric tons, is presently produced through the reaction of fossil-fuel-derived hydrogen and nitrogen (N_2) under high-temperature high-pressure conditions (Haber-Bosch method). Thus, new routes for sustainable ammonia synthesis are required. Excessive nitrate from overfertilization and industrial sewage is discharged into surface water and underground aquifers, threatening human health.[4] The electrocatalytic nitrate reduction reaction (NO_3^-RR) represents a viable approach with advantages in environmental restoration and energy economics under ambient conditions (Fig. 1a). Moreover, NO_3^-RR can be coupled with plasma/photocatalysis-driven nitrogen oxidation techniques to achieve conversion from air to ammonia.[5-8] Great progress has been made in the NO_3^-RR area from the points of fundamental research and practical application.[9-12] Very recently, an industrial-relevant current density (1 A cm^{-2}) for ammonia synthesis was reported with an onset potential of + 0.22 V versus a reversible hydrogen electrode (RHE).[9] Notably, the theoretical potential of the NO_3^-RR is + 0.69 V vs. RHE under alkaline conditions (pH=14),[13] much higher than the reported optimal onset potential.[14] Overlarge overpotentials will not only lose energy but also promote the competitive hydrogen evolution reaction (HER) and reduce the Faradaic efficiency (FE) of NH_3, resulting in dissatisfactory energy efficiency (EE) for NO_3^-RR. The high overpotential is caused by the sluggish rate-determining step of nitrate electroreduction to nitrite.[15] The rational design and construction of advanced electrocatalysts to overcome this issue based on the existing reaction mechanism is still challenging.

Theoretically, Co can undergo spontaneous redox with NO_3^- to produce $Co(OH)_2$ and NO_2^- with a Gibbs free energy change of -303.01 kJ/mol (Step 1 in Fig. 1b).[16] In this way, the rate-determining step from

nitrate to nitrite can be easily completed. Subsequently, $Co(OH)_2$ and NO_2^- can be reduced into Co and NH_3 through electrochemical and electrocatalytic processes, respectively, with the participation of active hydrogen (Steps 2 and 3 in Fig. 1b). Thus, the production of active hydrogen species is crucial for the designed three-step relay mechanism (spontaneous redox between Co and NO_3^-, $Co(OH)_2$ electroreduction to Co, and electrocatalytic NO_2^- to NH_3). According to the classic scaling relation, the adsorption energy of a hydrogen atom can be regarded as the descriptor for active hydrogen formation.[17] Ru, Rh, Pd, Ir, and Pt possess moderate adsorption energies for hydrogen atoms (Fig. 1c).[18-21] Among them, the cost of Ru is the lowest. Moreover, the hollow structure has been suggested to be conducive to mass transfer and atomic utilization in the electrocatalytic process.[22]

Herein, a series of Ru_xCo_y hollow nanododecahedrons (HNDs) are synthesized to carry out the designed three-step relay mechanism for NO_3^- electroreduction to ammonia. $Ru_{15}Co_{85}$ HNDs exhibit the highest performance with an onset potential of +0.4 V vs. RHE. Under optimal conditions, ammonia is generated at a rate as high as 3.21 ± 0.17 mol g_{cat}^{-1} h^{-1} with a corresponding FE of 96.78 ± 5.1 %. The energy consumption and production cost per kilo ammonia are calculated as 16.33 ± 0.68 kWh and $ 0.49 ± 0.02 at +0.3 V vs. RHE, which are both the lowest among all the reports. The high performance can be maintained under an industrial-relevant current density (1 A cm^{-2}) and a wide concentration range for nitrate (10-2000 mM), demonstrating the promising application potential. Furthermore, the combined results of *in situ* electrochemical isotope-labeled attenuated total reflection Fourier transformed infrared spectroscopy (ATR-FTIR), X-ray structure analysis (XAFS), Raman, X-ray diffraction (XRD), and theoretical simulation reveal the function of the three-step relay mechanism in decreasing the overpotential. The as-proposed three-step relay mechanism can also be extended to Ru_xFe_y and Ru_xNi_y for efficient NO_3^-RR to ammonia.

Results

Preparation and characterization of Ru_xCo_y HNDs. The catalysts of Ru_xCo_y HNDs are prepared via a two-step chemical conversion method, as displayed in Fig. 2a. First, dodecahedral ZIF-67 (Supplementary Fig. 1) react with different concentrations of Ru^{3+} and Co^{2+} under hydrothermal conditions, in which the hydrolysis process and the Kirkendall effect result in the formation of $Ru_xCo_yO_z$ HNDs with uniformly dispersed Ru and Co (Supplementary Figs. 2 – 3).[23–25] After annealing under a H_2 atmosphere, $Ru_xCo_yO_z$ HNDs are reduced into Ru_xCo_y while maintaining a hollow dodecahedral structure (Fig. 2b,c and Supplementary Fig. 4). The interplanar spacing of $Ru_{15}Co_{85}$ HNDs measured by high-resolution transmission electron microscopy (HRTEM) is 0.19 nm (Fig. 2d), corresponding to the (101) plane of the $Ru_{15}Co_{85}$ alloy.[26] XRD patterns show the shift of diffraction peaks to lower angles with increasing Ru content (Fig. 2e and Supplementary Fig. 5) due to the larger atomic radius of Ru than Co.[27] The calculated contents of Ru and Co based on the Vegard law and Bragg equation are close to the results of inductively coupled plasma optical emission spectrometry (ICP-OES) and energy dispersive spectroscopy

(EDS, Supplementary Table 1). Moreover, the surface content analysis of Ru and Co based on X − ray photoelectron spectroscopy (XPS, Supplementary Figs. 6,7 and Supplementary Tables 1,2) is also similar. The uniform distribution of high Ru content in Co originates from the confinement effect of the ZIF-67 porous structure to evenly store Ru^{3+} and Co^{2+} ions.[28] Locally enlarged XPS (Fig. 2f,g) shows that the binding energy of Ru^0 and Co^0 in Ru_xCo_y HNDs exhibit positive ($\Delta_{max,Ru}$ = 0.46 eV) and negative ($\Delta_{max,Co}$ = − 0.32 eV) shifts compared to pure Ru and Co, respectively, indicating electron transfer from Ru to Co.[29] This phenomenon is also confirmed by X-ray absorption fine structure (XAFS). The three-dimensional wavelet transforms of *K* − edge extended XAFS (Fig. 2h,i) exhibit the contoured feature with the maximum intensity as metallic Ru and Co in $Ru_{15}Co_{85}$ HNDs. The slight reverse shift of the absorption threshold of Ru and Co in $Ru_{15}Co_{85}$ HNDs (Supplementary Fig. 8) reveals the poor-electron and rich-electron states of Ru and Co, respectively.

Electrocatalytic NO_3^- RR performance over Ru_xCo_y. The hydrogen reversible reaction is first used to calibrate the reference electrode (Fig. 3a and Supplementary Fig. 9).[30] As illustrated in the linear sweep voltammetry (LSV) curves (Fig. 3b and Supplementary Fig. 10), the *j* of all catalysts shows significant increases after adding nitrate, implying the proceeding of NO_3^-RR over Ru_xCo_y HNDs. With increasing Ru content, the *j* values first increase and then decrease. $Ru_{15}Co_{85}$ HNDs exhibit the highest *j* and the lowest Tafel slope (Fig. 3c), implying the fastest electron transfer frequency for the NO_3^-RR. After the chronoamperometry measurements for NO_3^-RR (Supplementary Fig. 11), the products of nitrite and ammonia were analyzed and quantified by coloration and nuclear magnetic resonance (NMR) methods (Supplementary Figs. 12–14).[31] The plotted heatmaps (Fig. 3d, e and Supplementary Fig. 15a, b) intuitively exhibit the FE and $yield_{NH3}$ rate over Ru_xCo_y HNDs at given potentials. Among them, $Ru_{15}Co_{85}$ HNDs exhibit optimal performance. After normalization by the electrochemical surface area (ECSA) (Supplementary Figs. 15c,16,17 and Supplementary Note 1), $Ru_{15}Co_{85}$ HNDs still possess the highest performance for the NO_3^-RR under low overpotential, implying their high intrinsic activity. The onset potential over $Ru_{15}Co_{85}$ HNDs is + 0.4 V vs. RHE, close to the theoretical potential (+ 0.69 V vs. RHE).[13] Under + 0 V vs. RHE, ammonia is generated at a high FE of 96.78 ± 5.1% with a corresponding yield rate of 3.21 ± 0.17 mol g_{cat}^{-1} h^{-1}.[14] The energy efficiency (EE) for ammonia synthesis reveals an optimal value (41.54 ± 1.72%) at + 0.3 V vs. RHE for $Ru_{15}Co_{85}$ HNDs (Fig. 3f and Supplementary Fig. 18). For comparison, Co and $Ru_{15}Co_{85}$ nanoparticles (NPs) are prepared via the coprecipitation method. The results show that the HND structure can increase the number of active sites and promote the intrinsic activity of active sites for NO_3^-RR (Supplementary Figs. 18, 19 and Supplementary Note 2). Considering the upcoming industrialization of NO_3^-RR,[11,12] the cost of as-produced ammonia is significant. On the basis of the price of renewable electricity ($0.03 / kWh),[32] the energy consumption and production cost per kilo ammonia over $Ru_{15}Co_{85}$ HNDs are calculated as 16.33 ± 0.68 kWh and $ 0.49 ± 0.02, close to the commercial price ($0.58 ~ 1.02, sold in the USA).[33] Notably, this is a simple cost accounting based on electricity price, without considering capital costs and ohmic losses. Taking the environmental benefit of

nitrate contaminant removal into account, the reported $Ru_{15}Co_{85}$ HNDs for the NO_3^-RR show great attraction. Meanwhile, the pivotal performance parameters are summarized and compared with recently reported works (Fig. 3g and Supplementary Table 3). [10,13,14,34–36] The onset overpotential, EE, and ammonia price over $Ru_{15}Co_{85}$ HNDs are all the best as far as we know. Moreover, the high performance is maintained well in the continuous 30 cycles (Supplementary Fig. 21). After the chronoamperometry test, the three-dimensional skeleton structure, lattice spacing and Ru content are almost the same as those of the sample before the electrochemical test (Supplementary Fig. 22). These results indicate the high durability of $Ru_{15}Co_{85}$ HNDs for the NO_3^-RR. To further highlight the industrial production potential, a series of experiments are performed. First, the electrolyte with different NO_3^- concentrations (0.01-2 M) were studied, and the high performance was maintained well over a wide range (Fig. 3h). Then, a larger electrolytic cell equipped with a peristaltic pump to circulate the electrolyte is used for the NO_3^-RR test (see details in the Methods section and Supplementary Fig. 23a). The chronopotentiometry measurements can be operated over a wide range of current densities (50-1000 mA cm^{-2}, Supplementary Fig. 23b and Fig. 3i). The highest ammonia yield rate can achieve 3.83 ± 0.08 mmol cm^{-2} h^{-1} at 1000 mA cm^{-2}, and over 100 hours of long-term stability is obtained at 200 mA cm^{-2} (Fig. 3j). These results demonstrate the promising application potential of $Ru_{15}Co_{85}$ HNDs for the NO_3^-RR.

Mechanistic studies. After soaking $Ru_{15}Co_{85}$ HNDs in the electrolyte solution (0.1 M KOH and 0.1 M KNO_3), partial nitrate is converted to nitrite (Fig. 4a, Supplementary Fig. 24, and Supplementary Note 3). Similar phenomena can also be found for Co HNDs but are not suitable for Ru and $Ru_{15}Co_{85}O_z$ HNDs, implying the proceeding of spontaneous redox between Co^0 and NO_3^- to produce NO_2^-. The appearance of characteristic Raman peaks of Co-O bonds and XRD peaks (Supplementary Fig. 25) suggests the spontaneous formation of $Co(OH)_2$ (Eq. 1). The absence of Raman and XRD signals for Ru HNDs excludes its participation in the spontaneous redox process. The electrochemical *in situ* Raman spectra of $Ru_{15}Co_{85}$ HNDs show the disappearance of the Co-O characteristic peak (688 cm^{-1}) below 0 V vs. RHE (Fig. 4b), which is more positive than that of Co HNDs (− 0.5 V vs. RHE, Supplementary Fig. 26, 27).[30] These results demonstrate that redox-derived $Co(OH)_2$ species can be electroreduced *in situ* to metallic Co^0 (Eq. 2), and the existence of Ru can promote the electrochemical reduction process. The electrochemical *in situ* XRD characterization confirms the electroreduction of $Co(OH)_2$ into Co^0 (Fig. 4d). The first LSV curve of $Ru_{15}Co_{85}$ HNDs after soaking in NO_3^- electrolyte reveals that the $Co(OH)_2$ initial reduction potential starts from + 0.4 V vs. RHE (Fig. 4e), which corresponds to the onset potential of the NO_3^-RR over $Ru_{15}Co_{85}$ HNDs (+ 0.4 V vs. RHE, Fig. 3e and Supplementary Fig. 15b). Interestingly, this potential is more positive than the theoretical equilibrium potential of $Co^0/Co(OH)_2$ redox couple. One possible speculation is that the kinetic effect induced by the coupling of a chemical reaction to an electron transfer process causes the potential shift. Under constant electroreduction conditions, the characteristic Raman peak of $Co(OH)_2$ (688 cm^{-1}) intermittently appears and disappears with the addition of a small amount of nitrate and after the chronoamperometry reaction (Fig. 4f and

Supplementary Fig. 28), indicating the continuous proceeding of the redox reaction (Eq. 1) and the electroreduction reaction (Eq. 2). To further confirm this conclusion, electrochemical *in situ* XANES of $Ru_{15}Co_{85}$ HNDs (Fig. 4g) was performed. Co valence increases in the presence of nitrate. Taking the valence of Co in samples Co and CoO at 0.4 of normalized absorption as standards, we obtain the linear relation between valence state and *k*-edge energy of Co (black and yellow balls in Fig. 4h).[37] Co valences in $Ru_{15}Co_{85}$ HNDs under different conditions are determined (Fig. 4g,h, Supplementary Fig. 8b,29, and Supplementary Note 4). Interestingly, the nominal valence of Co in $Ru_{15}Co_{85}$ HNDs is + 0.87 and + 0.37 with nitrate under 0 V and − 0.5 V vs. RHE (-0.5 V is the most negative potential of our test range), respectively. However, the valence of Co in $Ru_{15}Co_{85}$ HNDs is − 0.16 without nitrate at 0 V vs. RHE. The indelible $Co^{\delta+}$ ($0 < \delta < 2$) indicates the oxidation of Co to $Co(OH)_2$ by nitrate (Eq. 1) and the electroreduction of $Co(OH)_2$ to Co (Eq. 2) simultaneously proceed during NO_3^-RR, and a dynamic Co-valence cycle is achieved.

$$NO_3^- + Co + H_2O \rightarrow NO_2^- + Co(OH)_2 \quad (1)$$

$$Co(OH)_2 + 2e^- \rightarrow Co + 2OH^- \quad (2)$$

$$NO_2^- + 5H_2O + 6e^- \rightarrow NH_3 + 7OH^- \quad (3)$$

Afterward, the nitrite electroreduction reaction (NO_2^-RR) to ammonia (Eq. 3) was studied by a mixed-isotopic labeling experiment (Fig. 4i). When we use equimolar $^{14}NO_3^-$ and $^{15}NO_3^-$ as the electrolyte, the generation of equimolar $^{14}NH_4^+$ and $^{15}NH_4^+$ can exclude the isotopic effect in the NO_3^-RR. Notably, only $^{14}NH_4^+$ is generated using equimolar $^{14}NO_2^-$ and $^{15}NO_3^-$ as the reactants, implying that NO_2^-RR occurs prior to NO_3^-RR. Meanwhile, the ammonia FE and yield rate both increase, especially in low overpotential regions (0.5 V to 0 V vs. RHE), by using nitrite to replace nitrate (Supplementary Fig. 30). These results demonstrate the advantage of the aforementioned three-step relay mechanism in decreasing the overpotential for the NO_3^-RR (Fig. 1). Moreover, this mechanism can also be extended to $Ru_{15}Ni_{85}$ and $Ru_{15}Fe_{85}$ HNDs, which both exhibit high performance for nitrate reduction to ammonia (Supplementary Figs. 31, 32).

The yield rate of ammonia in an alkaline environment ($pH \geq 7$) exhibits insensitive changes under different pH values, indicating the concerted proton-electron transfer (CPET) pathway for the hydrogenation process (Fig. 5a and Supplementary Fig. 33).[38] $Ru_{15}Co_{85}$ HNDs and Ru HNDs possess similar underpotential H deposition zones, while Co HNDs show no hydrogen zone in the test range (Supplementary Fig. 34). Moreover, electrochemical quasi-*in situ* electron paramagnetic resonance (EPR) reveals that the introduction of Ru is conducive to the formation of H radicals (Fig. 5b), implying the positive effect of Ru on active hydrogen formation. Subsequently, electrochemical isotope-labeling *in situ* ATR-FTIR spectra (Fig. 5c,d and Supplementary Figs. 35,36) and online DEMS (Fig. 5e) are adopted to capture possible intermediates. During the NO_2^-RR process (step 3), the characteristic peaks of $*^{14}NH_2$

(3190, 3037, and 1160 cm^{-1}) are detected and shifted to lower wavenumbers for $*^{15}NH_2$ (3157, 2987, and 1110 cm^{-1}) owing to the isotope effect. $*^{15}NO_2$ characteristic peak is centred at ~ 1250 cm^{-1}. Although the $*^{14}NO$ (~ 1610 cm^{-1}) characteristic peak overlaps with that of $*H_2O$ (1620 cm^{-1}), the negative shift of $*^{15}NO$ (~ 1552 cm^{-1}) indicates the existence of the *NO intermediate during the NO_2^-RR.[39,40] Notably, $Ru_{15}Co_{85}$ HNDs exhibit the same *in situ* ATR-FTIR spectra as Co HNDs but are quite different from Ru HNDs (Supplementary Fig. 35), implying that the active sites for NO_2^-RR lie in metal Co sites. The electrochemical *in situ* ATR-FTIR spectra of NO_3^-RR are similar to those of NO_2^-RR (Supplementary Fig. 36). Electrochemical online DEMS tests show the m/z signals of NO (30), NH_3 (17), N_2 (28), HNO (31), and NH_2OH (33) (Fig. 5e). On the basis of the aforementioned results, the possible reaction pathways for NO_2^-RR over $Ru_{15}Co_{85}$ HNDs, including dissociative, distal-O associative, distal-N associative and alternating-N associative, are deduced and summarized in Supplementary Fig. 37 and Supplementary Note 5.

Theoretical Simulation. Assuming the conversion from NO_3^- to NH_3 totally goes through CPET pathways, the minimum applied potential (*U*) of -0.28 V vs. RHE is required to generate ammonia thermodynamically, as marked by the vertical dotted line. The phase diagram of the abovementioned adsorbates on $Ru_{15}Co_{85}$ is presented as an example in Fig. 6a (Supplementary Note 6–7, Supplementary Fig. 38, and Supplementary Table 4). The transformation of *NO to *N is the potential-determinant step. The relationship among the applied potential/CPET steps/Ru ratio is presented in Fig. 6b (surface models are displayed in Supplementary Fig. 40). For almost all Ru_xCo_y samples (Supplementary Tables 5–8 and Note 8), the transformation of $*NO_3$ to *N demands negative applied potentials, especially for the *NO/*N couple (where the area is dark red with *U* between − 0.37 V ~ − 0.21 V vs. RHE), which implies that nitrate reduction through the pure electrochemical pathway is most likely thermodynamically limited by the N-O bond-breaking steps that demand negative applied potentials as low as − 0.37 V vs. RHE. However, such results contradict the experimental findings in Fig. 3e, where ammonia is already generated at $U > 0$ V vs. RHE. These findings indicate the existence of pathways other than the electrochemical method, especially for the N-O bond-breaking process. Figure 6c presents the as-proposed three-step relay pathway for $NO_3^-{}_{(aq)}$ reduction to ammonia. The reduction of $NO_3^-{}_{(aq)}$ to $NO_2^-{}_{(aq)}$ occurs through a redox reaction with Co^0, which is experimentally supported and matches well with the well-known findings that active metals reduce nitrate to nitrite in basic media.[41] The chemical cleavage of the N − O bond in $*NO_2$ and *NO is thermodynamically highly favored, with reaction Gibbs energies of − 2.0 eV and − 2.6 eV, respectively. The corresponding activation energies on the typical $Ru_{15}Co_{85}$ are 0.67 eV and 0.19 eV, respectively. The images of the various adsorbates and the related transition states (TS) are inserted in Fig. 6c. Interestingly, volcano-shaped curves for the adsorption of $*NH_2$ and *NO on various surfaces are observed, as shown in Fig. 6d, and Ru_7Co_{93} and $Ru_{15}Co_{85}$ are close to the top areas, which is coincident with the experimental findings (Fig. 3a-f) that these two alloys show better activity than the others.

In summary, we propose a three-step relay mechanism to decrease the reaction overpotential for the NO_3^-RR. A series of Ru_xCo_y HNDs catalysts are designed and prepared. $Ru_{15}Co_{85}$ HNDs exhibit the optimal catalytic performance (onset potential: +0.4 V vs. RHE, EE: 41.54 ± 1.72%, ammonia cost: $0.49 ± 0.02 /kg), outperforming all the reports. The electrochemical *in situ* ATR-FTIR, XAFS, Raman, XRD, and DFT calculations reveal that the high NO_3^-RR performance originates from the enhanced three-step relay processes on $Ru_{15}Co_{85}$ HNDs (spontaneous redox between Co and NO_3^-, $Co(OH)_2$ electroduction to Co and electrocatalytic NO_2^- to NH_3). The introduction of Ru can promote the electrocatalytic reduction of NO_2^- to ammonia and the electroreduction of $Co(OH)_2$ to Co benefiting from its excellent hydrogen supply capacity. Moreover, the efficient NO_3^-RR performance on $Ru_{15}Fe_{85}$ and $Ru_{15}Ni_{85}$ confirm the universality of the relay mechanism. This work provides a novel reaction pathway to improve the energy efficiency of the NO_3^-RR and inspires the design of efficient catalysts to extend to other electrocatalytic processes.

Methods

Material characterization. Scanning electron microscopy (SEM) images were taken with a Hitachi S-4800 scanning electron microscope. Transmission electron microscopy (TEM) images were obtained using a JEOL JEM-200 microscope. The X-ray diffraction (XRD) pattern was recorded with a Bruker D8 Focus Diffraction System by using a Cu *K*α source (λ = 0.154178 nm). X-ray photoelectron spectroscopy (XPS) spectra were collected on a Thermo Fisher Scientific K-Alpha + instrument using monochromatic Al Kα ($h\nu$ = 1486.6 eV) radiation. All spectra were collected at a vacuum pressure of < 2 ◊10^{-7} Pa, and the cumulative scanning number of each sample was 20. The sample was prepared and transferred into an Ar environment to avoid oxidation. All binding energies were referenced to the C 1*s* peak at 284.6 eV.[42] An inductively coupled plasma optical emission spectrometer (ICP-OES) was taken with an Agilent 7700x. For sample preparation, we dissolved 1 mg catalyst (0.5 mL of 2 mg mL^{-1} catalyst suspension) in 50 mL of aqua regia. After stirring overnight, KOH solution was used to adjust the pH to above 4, and then deionized water was used to dilute the concentration of ions. The ultraviolet-visible (UV-Vis) absorbance spectra were measured on a Beijing Purkinje General T6 new century spectrophotometer. Fourier transform infrared spectroscopy (FTIR) spectroscopy was carried out with a MAGNA1IR 750 (Nicolet Instrument) FTIR spectrometer. The EPR spectra were recorded on a Bruker EMX-8 spectrometer operated at 9.5 GHz 100 K. The NMR spectra were recorded on Varian Mercury Plus instruments at 600 MHz (1H NMR). The pH values of the electrolytes were determined using a pH meter (LE438 pH electrode, Mettler Toledo, USA). The Raman spectra were obtained on a Renishaw inVia reflex Raman microscope under an excitation of 532 nm laser light with a power of 20 mW. The XAFS was performed at the 1W1B beamline of the Beijing Synchrotron Radiation Facility (BSRF). The XAFS spectra were analyzed with the ATHENA software package. The *k*-weighting was set to 1 for the Fourier transforms. Fourier transforms of $\chi(k)$ were performed in the *k*-range of 2–8 $Å^{-1}$ with the Hanning window function. All the EXAFS spectra were obtained without phase correction. The signal acquisition time was 15–20 min for each scan. The XAS signal of powders was collected in transmission mode under ambient conditions. The powders were

uniformly coated on magic tape (2◊30 cm^2, produced by the Scotch company) and folded into a 2◊2 cm^2 sample.

XRD analysis. The lattice spacing can be calculated by the characteristic peaks of XRD based on the Bragg equation.

$$2d\sin\theta = n\lambda$$

Where *d* represents the lattice spacing and *θ* represents the angle between the incident ray and the crystal plane, corresponding to the characteristic peak angle of XRD. Notably, the abscissa of XRD (Fig. 2e) is 2*θ*. *n* is a natural number; here, we take *n* = 1. *λ* is the wavelength of the X-ray, and we take *λ* = 0.1544178 nm.

We calculated the content of Ru in the alloy by the Vegard law.

$$d = x_{\mathrm{Ru}}d_{\mathrm{Ru}} + x_{\mathrm{Co}}d_{\mathrm{Co}}$$

Here,$x_{\mathrm{Ru}} + x_{\mathrm{Co}} = 1$

Where *d*, $d_{Ru,}$ and d_{Co} represent the lattice spacings of the alloy, Ru, and Co, respectively. Among them, d_{Ru} and d_{Co} can be obtained by the Bragg equation of our catalysts (pure Ru and Co samples). x_{Ru} and x_{Co} are the molar contents of Ru and Co in the alloy, respectively.

The particle size can be calculated by the full width at half maximum (FWHM) of XRD based on the Debye-Scherrer equation.

$$D = \frac{K\lambda}{B\cos\theta}$$

Where *D* represents the particle size. *K* is the Scherrer constant; here, we take *K* = 0.89. B represents the FWHM of the XRD characteristic peak. *θ* represents the Bragg diffraction angle, *λ* is the wavelength of the X-ray, and we take *λ* = 0.1544178 nm. For the calculation of FWHM and particle size, we used the relevant functions in "*Jade 6*" software for integration and calculation.

Electrochemical NO_3^- RR measurements. Electrochemical NO_3^-RR measurements were performed with an Ivium – n–Stat electrochemical workstation (Ivium Technologies B.V.). A typical three-electrode H-cell was used, including a working electrode, an Ag/AgCl electrode (saturated KCl solution) as the reference electrode, and a carbon rod counter electrode in 0.1 M KOH or 0.1 M KNO_3 + 0.1 M KOH electrolyte, which was separated into a cathode cell (25 mL) and anode cell (30 mL) by an anion membrane (Alkymer AE-115). For catalytic potential, we do not use *iR* correction, except for special instructions. For the chronoamperometry test, carbon paper (0.5◊0.5 cm^2) decorated with 0.15 mg catalysts was used as the working electrode. In a typical procedure, an evenly distributed catalyst suspension was prepared by ultrasonically mixing 20 mg catalyst into 8 mL H_2O, 2 mL isopropyl alcohol, and 50 µL Nafion. The 75 µL suspension was covered on the carbon paper surface (0.25 cm^2). The current density was normalized by

the catalyst mass, the geometric area of the electrode, and the electrochemical surface area (ECSA). All electrochemical data (except stability testing) were repeated more than 3 times, and the error bar represents the standard deviation of the data. All potentials were calibrated to the reversible hydrogen electrode (RHE) by the following equation:

$$E_{\mathrm{RHE}} = E_{\mathrm{Ag/AgCl}} + 0.0591 \times \mathrm{pH} + \phi_{\mathrm{reference}}$$

Where $E_{Ag/AgCl}$ represents the experimental applied potential. Notably, the correction term (0.0591pH + $\varphi_{reference}$) is calibrated by a hydrogen reversible reaction (Fig. 3**a**, hydrogen evolution reaction and hydrogen oxidation reaction).

For the ECSA, we used the double-layer capacitance method in 0.1 M KOH solution during the non-Faradic potential range with different scan rates from 10 to 100 mV s^{-1}. The ECSA of the working electrodes was calculated according to the following equation:

$$I_{\mathrm{c}} = \upsilon C_{\mathrm{dl}}$$

$$ECSA = \frac{C_{\mathrm{dl}}}{C_{\mathrm{s}}}$$

Where I_c represents the charging current with different scan rates. v is the scan rate. C_{dl} is the double-layer capacitance. C_s represents the specific capacitance for a flat metallic surface, which is generally in the range of 20–60 μF cm^{-2}. According to the reports, we assume it is 40 μF cm^{-2}. [43–45]

The current density conversion formula from mass-normalized to geometric area-normalized is:

$$j_{\mathrm{geo.}} = \frac{j_{\mathrm{mass}} \times m}{S}$$

Where $j_{geo.}$ represents the current density normalized by geometric area, and j_{mass} represents the current density normalized by mass. m is the mass of the supported catalyst (0.15 mg). S is the carbon paper geometric area of the supported catalyst (0.25 cm^{-2}).

The linear voltammetry profile measurements were conducted under a flow of N_2 using the rotating disk electrode (RDE) deposited with the catalysts (40 μg) as the working electrode at a rotation rate of 100 ~ 1,600 rpm and a sweep rate of 2 mV·s^{-1}. All polarization curves were subjected to 80% *iR* correction.

Ammonia Faradaic efficiency was calculated according to the following equation:

$$\mathrm{FE_{NH3}} = \frac{Q_{\mathrm{NH3}}}{Q} = \frac{n_{\mathrm{NH3}} V c_{\mathrm{NH3}} F}{Q}$$

Where Q represents the applied overall coulomb quantity (C). Q_{NH3} represents the coulomb required to produce ammonia. n is the electron transfer number; for 1 mol ammonia, it is 8. V is the volume of the

catholyte of the cathode chamber, which is 25 mL. C_{NH3} is the concentration of ammonia produced. F is the Faraday constant (96,485 C•mol^{-1}).

The energy efficiency (EE) was defined as the ratio of fuel energy to applied electrical power, which was calculated with the following equation:

$$\mathrm{EE_{NH3}} = \frac{\left(E^{\theta}_{\mathrm{OER}} - E^{\theta}_{\mathrm{NH3}}\right) \times \mathrm{FE_{NH3}}}{E_{\mathrm{OER}} - E_{\mathrm{NH3}}}$$

Where E^{θ}_{NH3} represents the equilibrium potential of nitrate electroreduction to ammonia, which is 0.69 V vs. RHE under alkaline conditions. E^{θ}_{OER} represents the equilibrium potential of the oxygen evolution reaction, which is 1.23 V vs. RHE. FE_{NH3} is the Faradaic efficiency for ammonia. E_{OER} and E_{NH3} are the applied potentials (the overpotential of OER refers to the recently reported literature[46]).

For the amplified ammonia product process, we used chronopotentiometry to demonstrate the industrial application potential. Herein, the composition and type of electrolytic cell are the same as those of the previous chronoamperometry test, except that the volume of the electrolytic cell is changed to 80 mL. For the preparation of the electrode, carbon felt (0.5◊0.5 cm^2) decorated with 0.6 mg catalysts was used as the working electrode, and titanium mesh (1.5◊2 cm^2) was used as the counter electrode. A Ag/AgCl electrode (saturated KCl solution) was used as the reference electrode. Moreover, we employ a peristaltic pump to promote mass transfer, and the liquid circulation speed is 200 mL min^{-1}.

Electrochemical in situ **Raman tests.** The *in situ* Raman measurement was carried out by the aforementioned Raman microscope and electrochemical workstation. The cell was made up of a Teflon with a quartz window between the sample and the objective. The working electrode was immersed into the electrolyte through the wall of the cell, and the electrode plane was kept perpendicular to the laser. A platinum wire and Ag/AgCl served as the counter and reference electrodes, respectively. LSV curves were conducted from 0.5 to − 0.6 V vs. RHE with a scan rate of 2 mV s^{-1}. Electrochemical intermittent *in situ* Raman measurement was carried out in 0.1 M KOH solution under + 0.3 V vs. RHE. After collecting the first Raman spectrum, we added 1 ml 0.1 M KNO_3 solution to the electrolyte. After 1 min, we collected the second Raman spectrum. After 20 min, nitrate was totally reduced, and then the Raman spectrum was collected again. We repeated this cycle test 4 times.

Electrochemical in situ **ATR-FTIR tests.** Electrochemical *in situ* ATR-FTIR measurements were performed on a Linglu Instruments ECIR-II cell mounted on a Pike Veemax III ATR with a single bounce silicon crystal covered with an Au membrane in internal reflection mode. Spectra were recorded on a Thermo Nicolet Nexus 670 spectrometer. The electrolyte was degassed by bubbling N_2 for 30 min before the measurement. The single-bounce silicon crystal covered with a Au membrane was prepared through the following procedure. (1) 0.12 g NaOH, 0.23 g $NaAuCl_4{\cdot}2H_2O$, 0.13 g NH_4Cl, 0.95 g Na_2SO_3, and 0.62 g $Na_2S_2O_3{\cdot}5H_2O$ were dissolved in 100 mL H_2O (denoted as Solution A). (2) Monocrystal silicon was

immersed in aqua regia ($V_{\text{concentrated HCl}}$:$V_{HNO3}$ = 1:1) for 20 min and then polished using Al powder for 10 min. After washing three times with water and acetone, clean monocrystal silicon was obtained. (3) The above monocrystal silicon was immersed in a mixture of H_2SO_4 and H_2O_2 ($V_{\text{concentrated H2SO4}}$: V_{H2O2} = 1:1) for 20 min. (4) After washing three times with water, the above monocrystal silicon was then immersed in 40% NH_4F aqueous solution and washed three times with water. (5) Monocrystal silicon was immersed in a mixture of 15 mL solution A and 3.4 mL 2% NH_4F aqueous solution. (6) After 5 min, Au-coated monocrystal silicon was obtained.

Electrochemical online DEMS test. 0.1 M KOH + 0.1 M KNO_3 electrolyte kept flowing into a homemade electrochemical cell through a peristaltic pump. Glassy carbon electrodes coated with $Ru_{15}Co_{85}$ HNDs catalyst, Pt wire, and Ag/AgCl electrodes were used as the working electrode, counter electrode, and reference electrode, respectively. Then, the applied voltage (− 0.2 V vs. RHE) was employed alternately, and the interval was 2 minutes. After the electrochemical test was over and the mass signal returned to baseline, the next cycle started using the same conditions to avoid accidental error. After seven cycles, the experiment ended.

Electrochemical in situ **XAS test.** Electrochemical *in situ* XAS at the Co K-edge was carried out at the 1W1B beamline of the Beijing Synchrotron Radiation Facility (BSRF). The electrolytic cell was made in-house with Teflon containing 0.1 M KOH or 0.1 M KOH + 0.1 M KNO_3 electrolyte, in which a graphite rod and Ag/AgCl electrode were used as the counter electrode and reference electrode, respectively. Carbon paper (2◊2 cm^2) loaded with an electrocatalyst (3 mg) was used as the working electrode, and the catalyst was concentrated in the center of the carbon paper with an effective area of more than 1 cm^2. The *in situ* XAS signal was collected in fluorescence mode at chronoamperometry measurement with 0 V or − 0.5 V vs. RHE. No pretreatment was required before the electrochemical chronoamperometry test.

Electrochemical in situ **XRD test.** Electrochemical *in situ* XRD patterns were measured on a Rigaku Smartlab9KW Diffraction System using a Cu Kα source (λ = 0.15406 nm). The electrolytic cell was made up of Teflon with Pt wire as the counter electrode and a Hg/HgO electrode as the reference electrode. Carbon paper (0.5◊0.5 cm^2) loaded with catalyst (0.6 mg) was used as the working electrode, and the patterns were collected under chronoamperometry measurement under different potentials. Before collecting data, we ran the chronoamperometry test under the applied potential for 5 min. The pattern was collected in the 2θ ranging from 20° to 70° under the applied potential from − 0.4 V to 0.5 V vs. RHE. Each diffraction pattern was collected for 5 min for statistical analysis.

Other experimental details have been added to the **Supplementary Methods**, including Materials, Preparation of catalysts, Materials characterizations, determination and quantitation of ammonia/nitrite, and computational methods.

Online content

Any methods, additional references, Nature Research reporting summaries, source data, extended data, supplementary information, acknowledgments, peer review information; details of author contributions and competing interests; and statements of data and code availability are available at https://doi.org/xxxxxx.

Declarations

Data availability

The data that support the findings of this study are available from the corresponding authors.

Correspondence and requests for materials should be addressed to Bin Zhang.

Acknowledgment

We acknowledge the National Natural Science Foundation of China (Nos. 22071173(Y.Y.), 22271213(B.Z.), and 21871206(B.Z.)) and the Natural Science Foundation of Tianjin City (No. 20JCJQJC00050(Y.Y.)). We do appreciate Ms. Yang Liu in the Analysis and Testing Center at Tianjin University for in situ ATR-FTIR assistance and the 1W1B beamline of the Beijing Synchrotron Radiation Facility for supporting this work.

Author Contributions

B. Z. and Y. Y. conceived the idea and supervised the project. B.Z., Y.Y., and S.H. designed the experiments. S.H. synthesized the materials and carried out electrochemical measurements. H.L. and R.Y. performed theoretical calculations. S.H. and T.L. carried out *in situ* experiments. S.H. and F.C. drew the schematic diagram. B.Z., Y.Y., and S.H. wrote the paper with comments from all authors.

Additional information

Supplementary information The online version contains supplementary material available at https://doi.org/xxxxxxx.

Reprints and permissions information is available at http://www.nature.com/reprints.

Competing Financial Interests

The authors declare no competing interests.

References

1. Van Langevelde, P. H., Katsounaros, I. and Koper, M. T. Electrocatalytic nitrate reduction for sustainable ammonia production. *Joule* **5**, 290–294 (2021).

2. Christensen, C. H., Johannessen, T., Sørensen, R. Z. and Nørskov, J. K. Towards an ammonia-mediated hydrogen economy? *Catal. Today* **111**, 140–144 (2006).
3. Van der Ham, C. J., Koper, M. T. and Hetterscheid, D. G. Challenges in reduction of dinitrogen by proton and electron transfer. *Chem. Soc. Rev.* **43**, 5183–5191 (2014).
4. Rogan, W. J. & Brady, M. T. Drinking water from private wells and risks to children. *Pediatrics* **123**, e1123–e1137 (2009).
5. Li, L. *et al.* Efficient nitrogen fixation to ammonia through integration of plasma oxidation with electrocatalytic reduction. *Angew. Chem.* **60**, 14131-14137 (2021).
6. Sun, J. *et al.* A hybrid plasma electrocatalytic process for sustainable ammonia production. *Energy Environ. Sci.* **14**, 865-872 (2021).
7. Yuan, S. *et al.* Nitrate formation from atmospheric nitrogen and oxygen photocatalysed by nano-sized titanium dioxide. *Nat. Commun.* **4**, 2249 (2013).
8. Yu, Y., Wang, C., Yu, Y., Wang, Y. & Zhang, B. Promoting selective electroreduction of nitrates to ammonia over electron-deficient Co modulated by rectifying Schottky contacts. *Sci. China Chem.* **63**, 1469-1476 (2020).
9. Chen, F. *et al.* Efficient conversion of low-concentration nitrate sources into ammonia on a Ru-dispersed Cu nanowire electrocatalyst. *Nat. Nanotechnol.* **17**, 759–767 (2022).
10. Chen, G. *et al.* Electrochemical reduction of nitrate to ammonia via direct eight-electron transfer using a copper–molecular solid catalyst. *Nat. Energy* **5**, 605-613 (2020).
11. Wang, A. *et al.* Electrochemistry-stimulated environmental bioremediation: Development of applicable modular electrode and system scale-up. *Environ. Sci. Ecotechnol.* **3**, 100050 (2020).
12. Zheng, W. *et al.* Self-activated Ni cathode for electrocatalytic nitrate reduction to ammonia: from fundamentals to scale-up for treatment of industrial wastewater. *Environ. Sci. Technol.* **55**, 13231-13243 (2021).
13. Wang, Y. *et al.* Enhanced nitrate-to-ammonia activity on copper–nickel alloys via tuning of intermediate adsorption. *J. Am. Chem. Soc.* **142**, 5702–5708 (2020).
14. Li, J. *et al.* Efficient ammonia electrosynthesis from nitrate on strained ruthenium nanoclusters. *J. Am. Chem. Soc.* **142**, 7036–7046 (2020).
15. Dima, G. E., de Vooys, A. C. A. and Koper, M. T. M. Electrocatalytic reduction of nitrate at low concentration on coinage and transition-metal electrodes in acid solutions. *J. Electroanal. Chem.* **554–555**, 15–23 (2003).
16. Gatla, S. *et al.* Impact of Co-components on the state of Pd and the performance of supported Pd/TiO_2 catalysts in the gas-phase acetoxylation of toluene. *ChemCatChem* **3**, 1893–1901 (2011).
17. Nørskov, J. K. *et al.* Trends in the exchange current for hydrogen evolution. *J. Electrochem. Soc.* **152**, J23 (2005).
18. Seh, Z. W. *et al.* Combining theory and experiment in electrocatalysis: Insights into materials design. *Science* **355** eaad4998 (2017).

19. Thomas F. Jaramillo, K. P. J., Jacob Bonde, Jane H. Nielsen, Sebastian Horch, Ib Chorkendorff. Identification of active edge sites for electrochemical H_2 evolution from MoS_2 nanocatalysts. *Science* **317**, 100–102 (2007).
20. Miao, M. *et al.* Molybdenum carbide-based electrocatalysts for hydrogen evolution reaction. *Chem. Eur. J.* **23**, 10947–10961 (2017).
21. Hoster, H. E. Anodic hydrogen oxidation at bare and Pt-modified Ru(0001) in flowing electrolyte-theory versus experiment. *MRS Proceedings* **1388** (2012).
22. Tian, X. *et al.* Engineering bunched Pt-Ni alloy nanocages for efficient oxygen reduction in practical fuel cells. *Science* **366**, 850–856 (2019).
23. Yu, Y., Shi, Y. and Zhang, B. Synergetic transformation of solid inorganic-organic hybrids into advanced nanomaterials for catalytic water splitting. *Acc. Chem. Res.* **51**, 1711–1721 (2018).
24. Chee, S. W., Tan, S. F., Baraissov, Z., Bosman, M. & Mirsaidov, U. Direct observation of the nanoscale Kirkendall effect during galvanic replacement reactions. *Nat. Commun.* **8**, 1224 (2017).
25. Liu, Z. *et al.* Tuning infrared plasmon resonances in doped metal-oxide nanocrystals through cation-exchange reactions. *Nat. Commun.* **10**, 1394 (2019).
26. Zhu, T. *et al.* High-index faceted RuCo nanoscrews for water electrosplitting. *Adv. Energy Mater.* **10**, 2002860 (2020).
27. He, T. *et al.* Mastering the surface strain of platinum catalysts for efficient electrocatalysis. *Nature* **598**, 76–81 (2021).
28. Zhuang, Z. *et al.* Three-dimensional open nano-netcage electrocatalysts for efficient pH-universal overall water splitting. *Nat. Commun.* **10**, 4875 (2019).
29. Biesinger, M. C. *et al.* Resolving surface chemical states in XPS analysis of first row transition metals, oxides and hydroxides: Cr, Mn, Fe, Co and Ni. *Appl. Surf. Sci.* **257**, 2717-2730 (2011).
30. Niu, S., Li, S., Du, Y., Han, X. and Xu, P. How to Reliably Report the Overpotential of an Electrocatalyst. *ACS Energy Lett.* **5**, 1083-1087 (2020).
31. Hodgetts, R. Y. *et al.* Refining universal procedures for ammonium quantification via rapid ^{1}H NMR analysis for dinitrogen reduction studies. *ACS Energy Lett.* **5**, 736-741 (2020).
32. Xia, C. *et al.* Confined local oxygen gas promotes electrochemical water oxidation to hydrogen peroxide. *Nat. Catal.* **3**, 125–134 (2020).
33. *Natural gas prices only account for 15% of run-up in anhydrous ammonia prices, Shows New Texas A&M Study*, <https://www.agweb.com/news/crops/corn/natural-gas-prices-only-account-15-run-anhydrous-ammonia-prices-shows-new-texas-am>
34. Wang, Y., Zhou, W., Jia, R., Yu, Y. and Zhang, B. Unveiling the activity origin of a copper-based electrocatalyst for selective nitrate reduction to ammonia. *Angew.Chem.* **59**, 5350-5354 (2020).
35. Wang, Z., Young, S. D., Goldsmith, B. R. and Singh, N. Increasing electrocatalytic nitrate reduction activity by controlling adsorption through PtRu alloying. *J. Catal.* **395**, 143-154 (2021).

36. Liu, H. *et al.* Efficient electrochemical nitrate reduction to ammonia with copper-supported rhodium cluster and single-atom catalysts. *Angew. Chem.* **61**, e202202556 (2022).
37. Zhou, Y. *et al.* Lattice-confined Ru clusters with high CO tolerance and activity for the hydrogen oxidation reaction. *Nat. Catal.* **3**, 454–462 (2020).
38. Koper, M. T. M. Theory of multiple proton-electron transfer reactions and its implications for electrocatalysis. *Chem. Sci.* **4**, 2710-2723 (2013).
39. Yao, Y., Zhu, S., Wang, H., Li, H. and Shao, M. A spectroscopic study on the nitrogen electrochemical reduction reaction on gold and platinum surfaces. *J. Am. Chem. Soc.* **140**, 1496–501 (2018).
40. Katsounaros, I. *et al.* On the mechanism of the electrochemical conversion of ammonia to dinitrogen on Pt (100) in alkaline environment. *J. Catal.* **359**, 82–91 (2018).
41. Fanning, J. C. The chemical reduction of nitrate in aqueous solution. *Coordin. Chem. Rev.* **199**, 159–179 (2000).
42. Tufts, B. J. *et al.* XPS and EXAFS studies of the reactions of cobalt (III) ammine complexes with gallium arsenide surfaces. *J. Am. Chem. Soc.* **112**, 5123-5136 (1990).
43. McCrory, C. C., Jung, S., Peters, J. C. & Jaramillo, T. F. Benchmarking heterogeneous electrocatalysts for the oxygen evolution reaction. *J. Am. Chem. Soc.* **135**, 16977-16987 (2013).
44. Wu, J. *et al.* Densely populated isolated single Co-N site for efficient oxygen electrocatalysis. *Adv. Energy Mater.* **9**, 1900149 (2019).
45. McCrory, C. C. *et al.* Benchmarking hydrogen evolving reaction and oxygen evolving reaction electrocatalysts for solar water splitting devices. *J. Am. Chem. Soc.* **137**, 4347-4357 (2015).
46. Wang, J. *et al.* Redirecting dynamic surface restructuring of a layered transition metal oxide catalyst for superior water oxidation. *Nat. Catal.* **4**, 212-222 (2021).

Figures

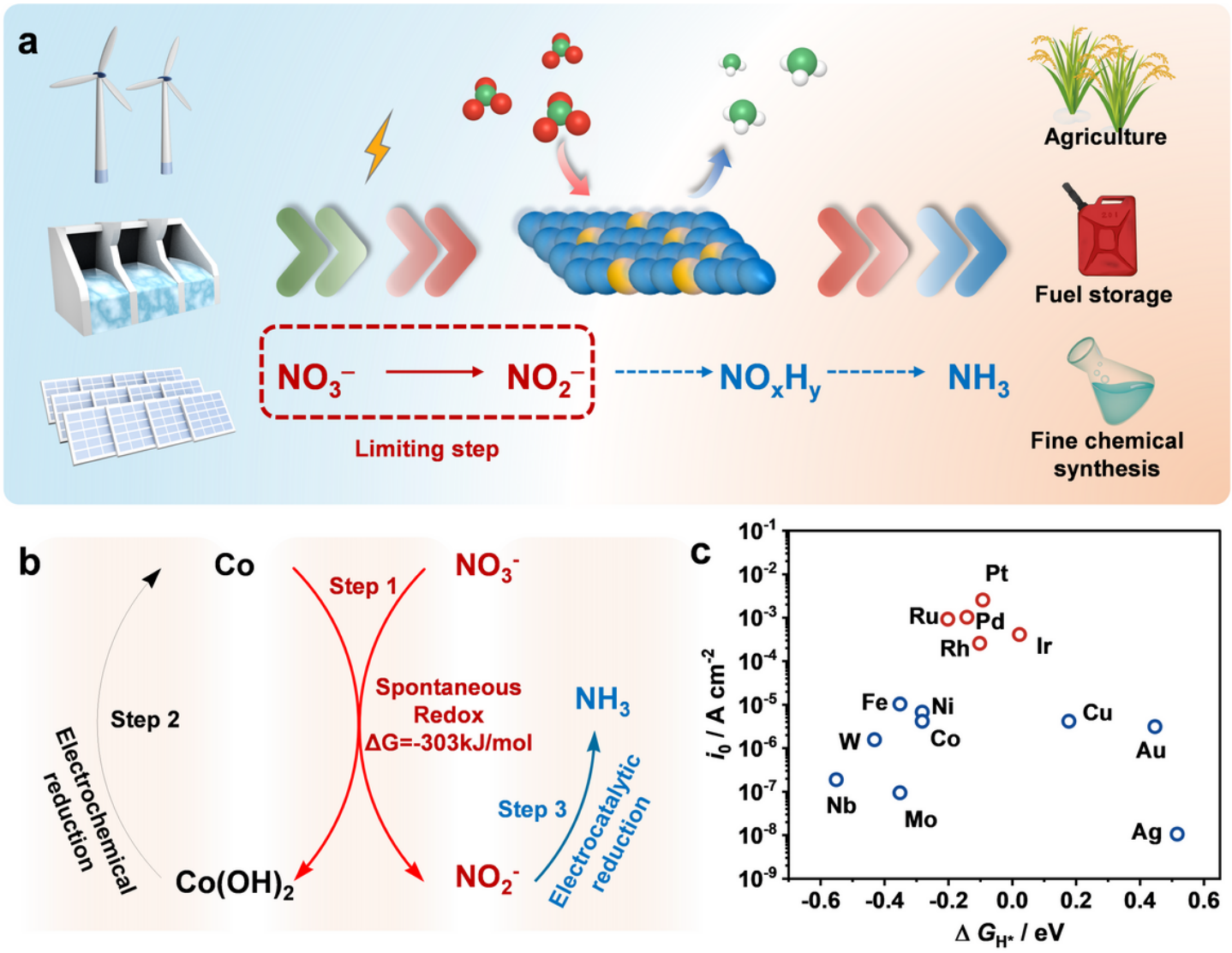

Figure 1

Catalyst design for the NO_3^-RR. a, Schematic illustration of the electrochemical NO_3^-RR to NH_3 under ambient conditions using renewable energy. **b,** The designed three-step relay mechanism for the NO_3^-RR. **c**, Volcano plot of the exchange current density and Gibbs free energy of adsorbed atomic hydrogen for different metals.

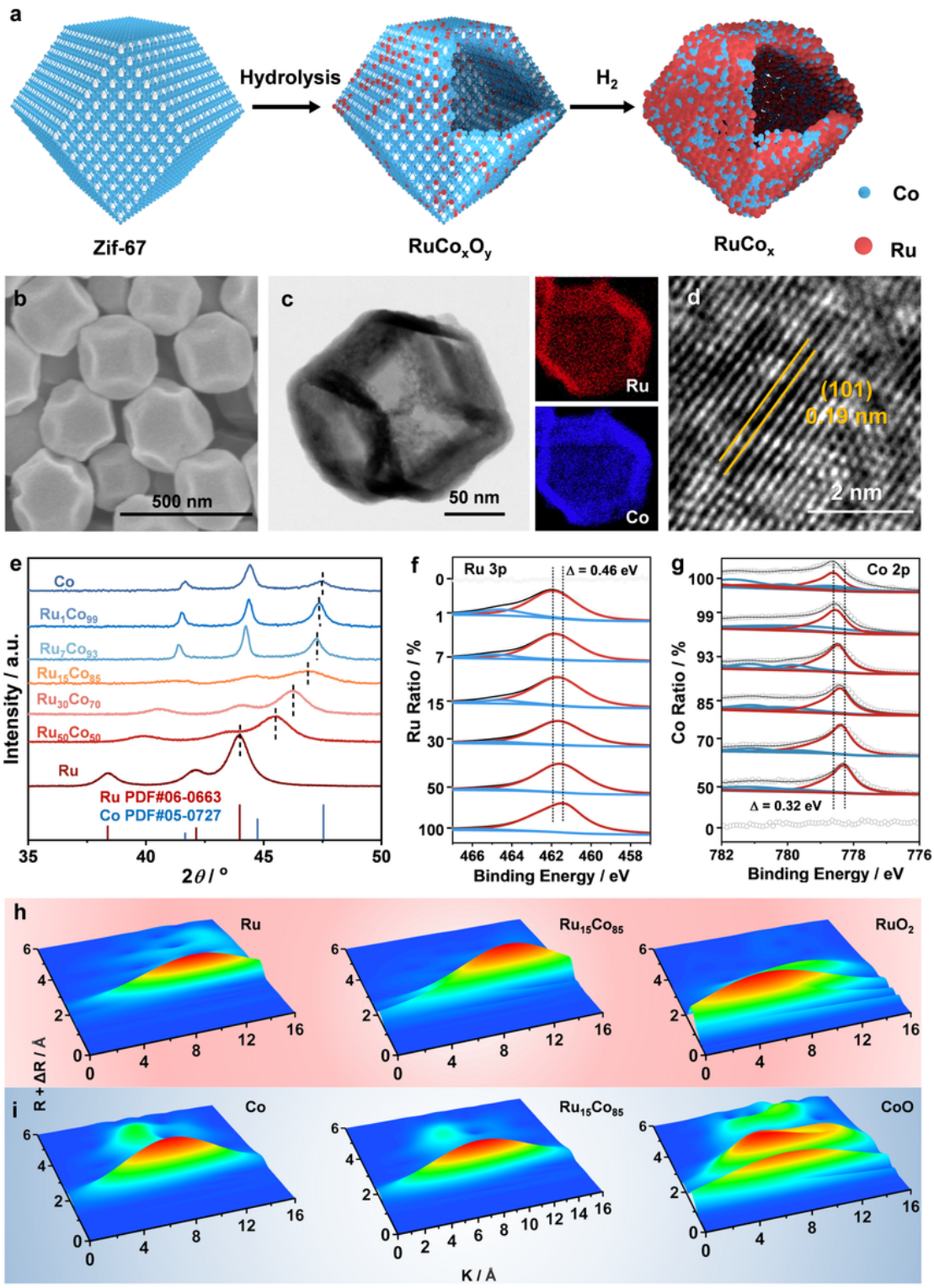

Figure 2

Structural characterization of $Ru_xCo_yO_z$ and Ru_xCo_y HNDs. a, Schematic illustration of Ru_xCo_y HNDs synthesis. **b**, **c**, **d**, SEM (**b**), TEM and corresponding EDS mapping (**c**), and HRTEM (**d**) images of $Ru_{15}Co_{85}$ HNDs. **e**,**f**,**g**, Locally enlarged XRD patterns (**e**) and XPS spectra (**f** and **g**) of Ru_xCo_y HNDs. **h, i,** Wavelet

transforms of Ru (**h**) and Co (**i**) for the k^3–weighted XAFS signals in $Ru_{15}Co_{85}$ HNDs and contrast samples.

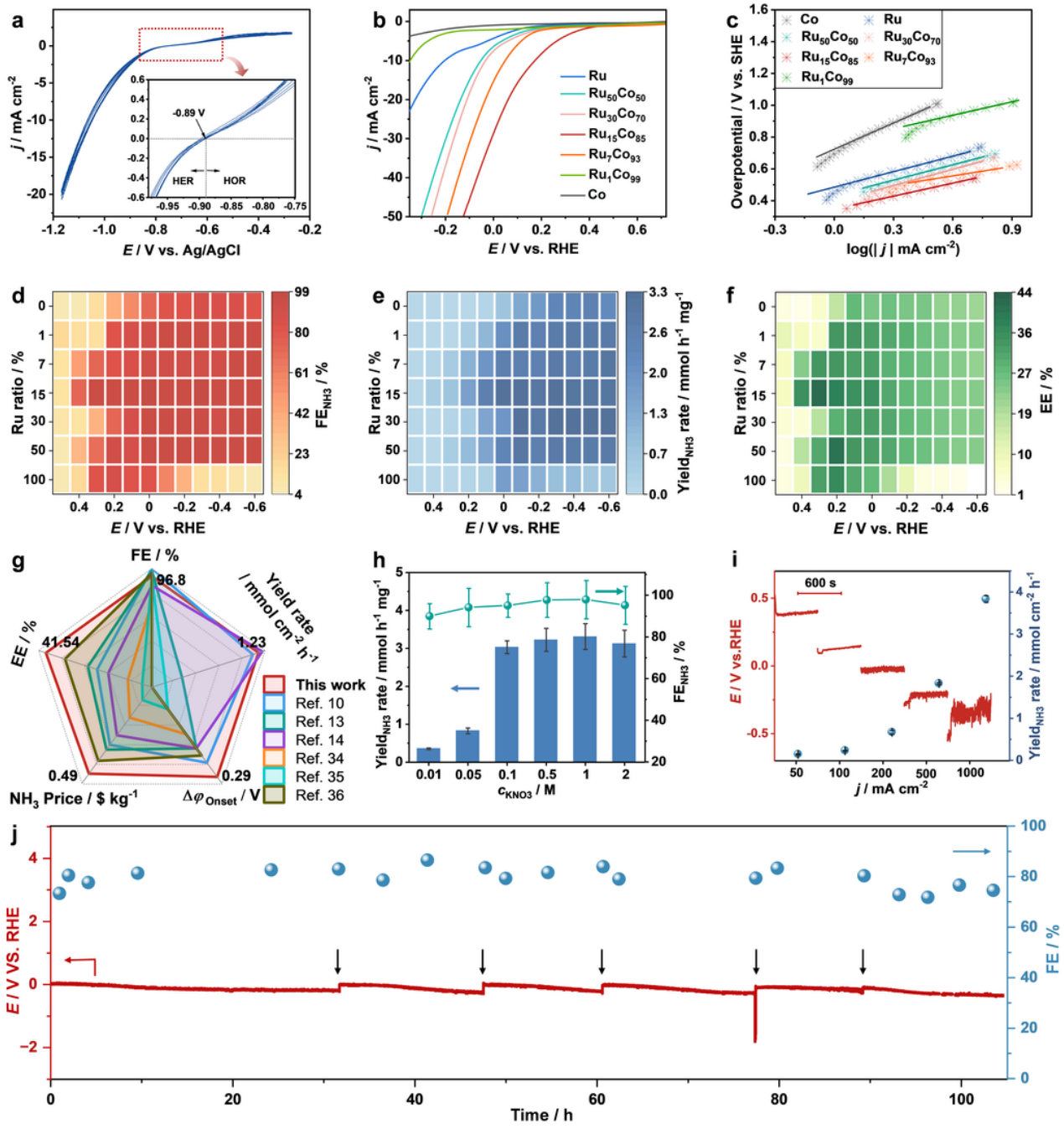

Figure 3

Electrocatalytic performance for the NO_3^-RR. a, CV curves of Ag/AgCl electrode calibration in 0.1 M KOH solution. **b,** LSV curves of NO_3^-RR over Ru_xCo_y HNDs under 1600 rpm with 80% *iR* correction. **c,** Tafel slopes of NO_3^-RR over Ru_xCo_y HNDs. **d**, **e**, **f**, Heatmaps of FE (**d**), yield rate (**e**), and EE (**f**) for ammonia synthesis over Ru_xCo_y HNDs. **g,** Comparison of NO_3^-RR performance over $Ru_{15}Co_{85}$ HNDs with recently

reported catalysts. **h,** The NO_3^-RR performance over $Ru_{15}Co_{85}$ HNDs at different concentrations of KNO_3. **i,** Chronopotentiometry curves and ammonia yield rate of NO_3^-RR (0.1 M KNO_3 + 0.1 M KOH) over $Ru_{15}Co_{85}$ HNDs at different current densities with 80% *iR* correction on potential. **j**, Long-term electrocatalytic stability test of NO_3^-RR (0.1 M KNO_3 + 0.1 M KOH) over $Ru_{15}Co_{85}$ HNDs at 200 mA cm^{-2} using a continuous flow system in an H-cell. The black arrow represents the renewal of fresh electrolytes.

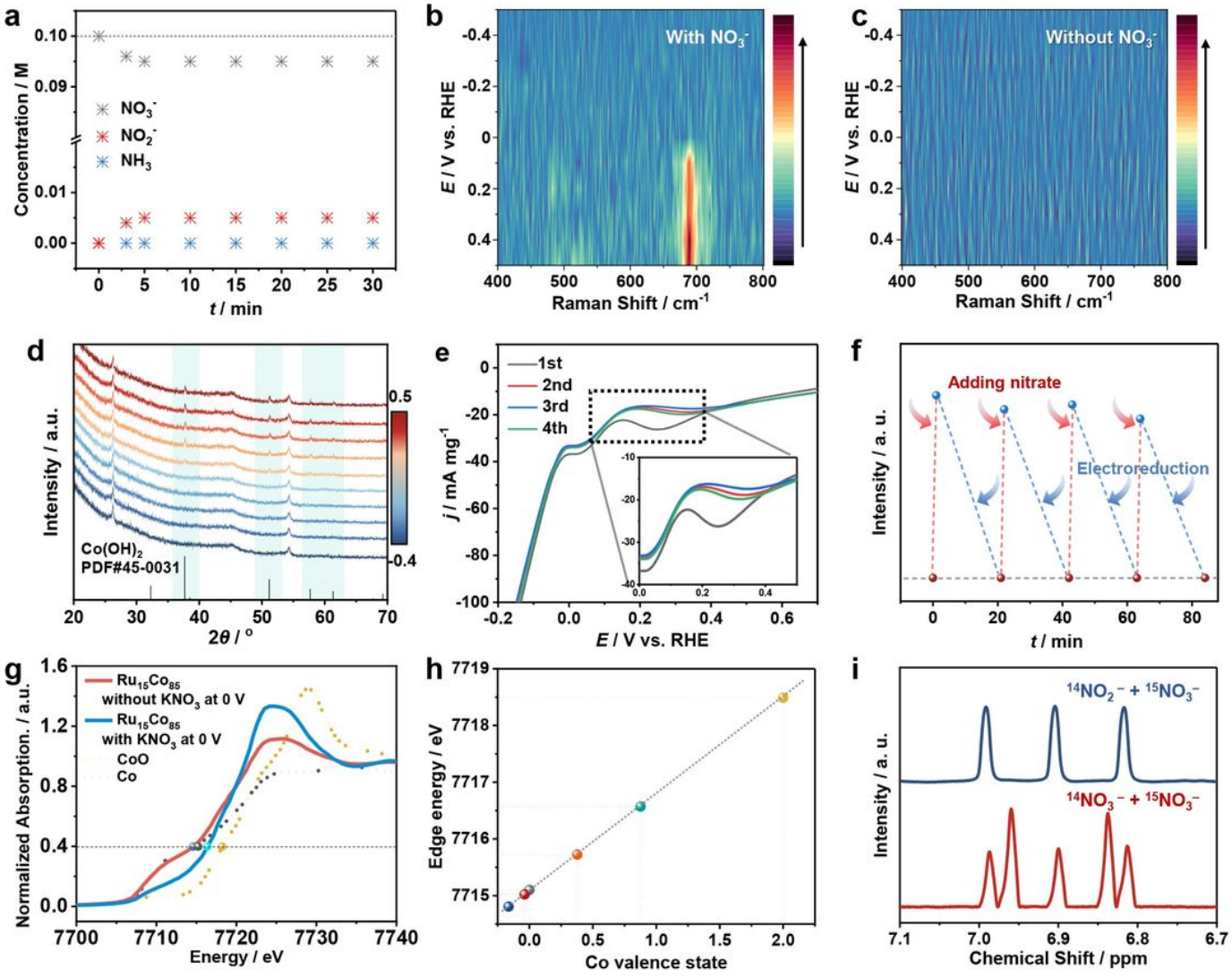

Figure 4

Mechanistic studies for NO_3^-RR over $Ru_{15}Co_{85}$ HNDs. a, The concentration variation of NO_3^-, NO_2^-, and NH_3 in the electrolyte after the redox reaction with $Ru_{15}Co_{85}$ HNDs for different times without an applied potential. **b**,**c**, Electrochemical *in situ* Raman spectra of $Ru_{15}Co_{85}$ HNDs with (**b**) and without (**c**) NO_3^-. **d,** Electrochemical *in situ* XRD patterns of NO_3^-RR over $Ru_{15}Co_{85}$ HNDs. The * represents the characteristic peak of $Co(OH)_2$ (PDF # 45-0031), corresponding to (002), (102), (110), and (111) of hexagonal phase P-3m1. **e,** Continuous LSV curves of $Ru_{15}Co_{85}$ in 0.1 M KOH solution. The $Ru_{15}Co_{85}$ sample was first

soaked in NO_3^- electrolyte for 10 minutes and then washed with distilled water for 10 minutes. **f,** The intermittent *in situ* Raman peak intensity at 688cm^{-1} over $Ru_{15}Co_{85}$ HNDs at +0.3 V vs. RHE for the NO_3^-RR with alternate conditions of NO_3^- consumption and NO_3^- addition. **g,** Electrochemical *in situ* XANES of $Ru_{15}Co_{85}$ and *ex situ* XANES of standard samples (Co and CoO). **h,** Relation between the Co L_3-edge absorption energy and valence states. **i,** ^{1}H NMR of NH_4^+ in the mixed isotope labeling experiments.

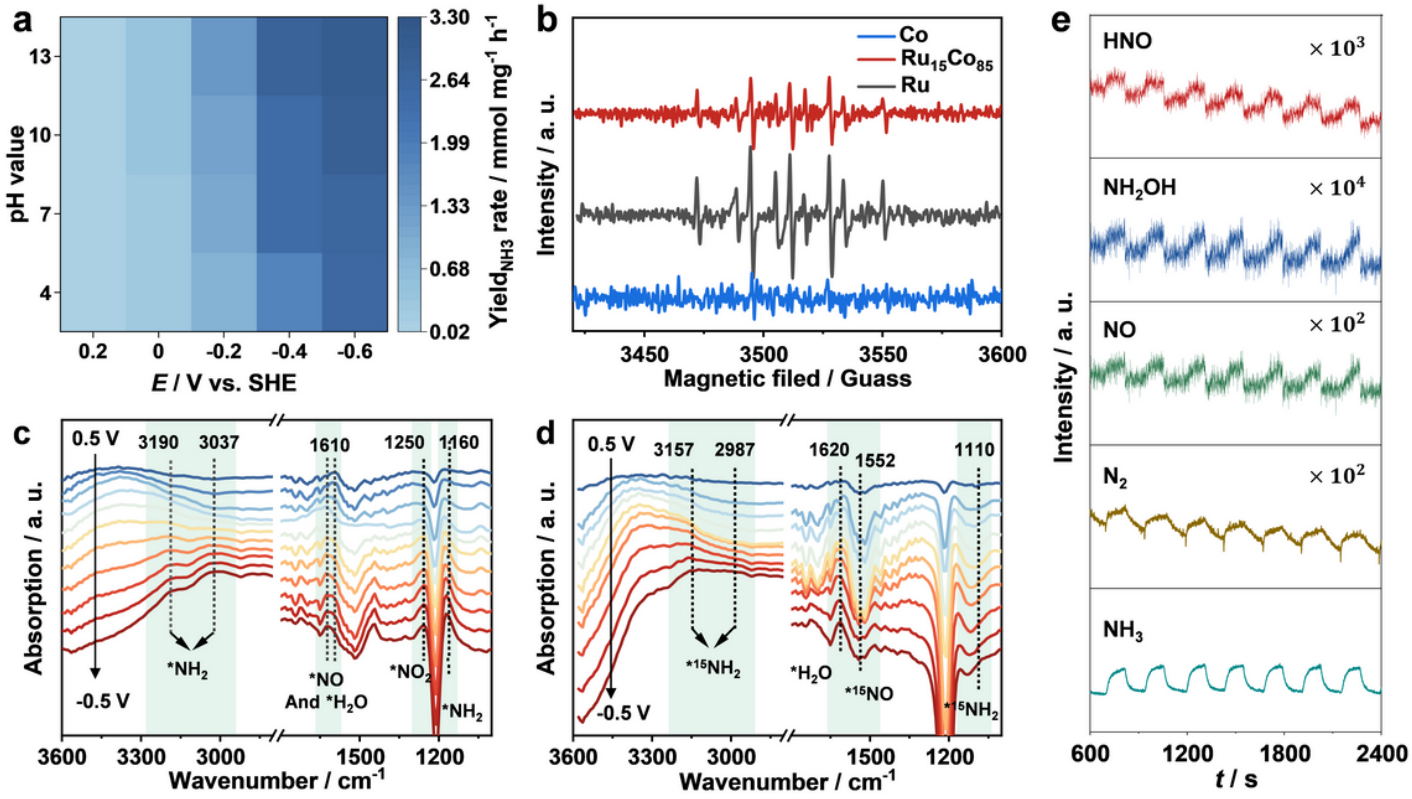

Figure 5

NO_3^-RR pathway over $Ru_{15}Co_{85}$ HNDs. a, Yield rate of NH_3 in different pH buffer solutions. **b**, Electrochemical quasi-*in situ* EPR tests at 0 V vs. RHE. **c, d**, Isotope-labeling electrochemical *in situ* ATR-FTIR spectra of $Ru_{15}Co_{85}$ HNDs using $^{14}NO_2^-$ (**c**) and $^{15}NO_2^-$ (**d**) as reactants. **e**, Electrochemical online DEMS of NO_3^-RR over $Ru_{15}Co_{85}$.

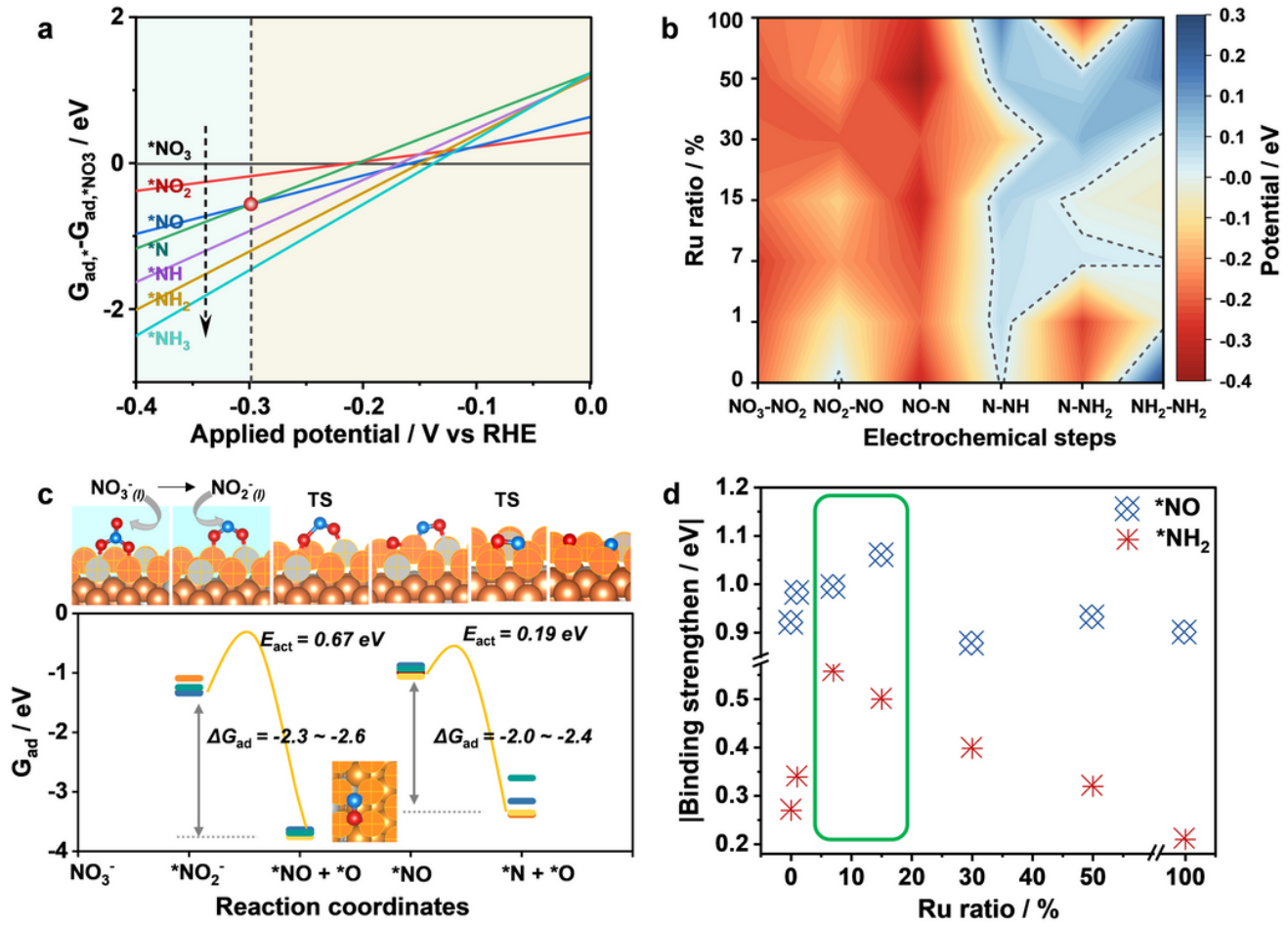

Figure 6

Theoretical calculation results for NO3−RR. a, Phase diagram of various adsorbates on Ru15Co85. The vertical dotted line indicates the minimum applied potential required to reach thermodynamic feasibility. **b**, Mapping of the minimum applied potential required to reach the thermodynamic feasibility of various electrochemical transfer steps on RuxCoy surfaces. **c**, The activation and reaction energies of the N−O bond breaking elementary steps. The inserted images show the corresponding adsorption geometries and transition states on Ru15Co85 (101). **d**, The binding strength of *NO and *NH2 on RuxCoy surfaces. The ordinate is the absolute value of Binding strengthen.

Supplementary Files

This is a list of supplementary files associated with this preprint. Click to download.

- HSHSupplementaryInformation.pdf